Journal of Positive Sciences (JPS) eISSN: 2582-9351, https://positive-sciences.com JPS. 2026 Jun; 6(4): 49-68

Article info
Received on: 01.05.2026
Accepted on: 01.06.2026
Published on: 11.06.2026
doi: https://doi.org/10.52688/ASP54999

Research Article

Effect of Cu Doping on the Structural, Vibrational, Thermal, and Densification Properties of Sol–Gel Derived ZnO Nanoceramics

Mojahid M. Najim [1], Ban A. Yousif [2], Duraid F. Mahdi [3], Mohammed RASHEED [4, *]

[1] Nanomaterials Research Center, University Of Anbar, Ramadi, Iraq
[2, 3] College of Applied Sciences, University of Technology- Iraq, Baghdad, Iraq
[4] Production Engineering & Metallurgy College, University of Technology- Iraq, Baghdad 10066, Iraq

[*] rasheed.mohammed40@yahoo.com

ABSTRACT

Pure and Cu-doped ZnO nanoceramic pellets containing 0, 2, 4, and 6 wt.% Cu were successfully synthesized via the sol–gel method, compacted into pellets, and sintered at 1000 °C. The influence of Cu incorporation on the structural, vibrational, thermal, densification, and chemical stability properties of ZnO nanoceramics was systematically investigated using X-ray diffraction (XRD), Fourier-transform infrared spectroscopy (FTIR), Raman spectroscopy, density and porosity measurements, thermogravimetric analysis (TGA), derivative thermogravimetry (DTG), differential scanning calorimetry (DSC), and inductively coupled plasma optical emission spectroscopy (ICP–OES). XRD analysis confirmed the formation of a single-phase hexagonal wurtzite ZnO structure (JCPDS No. 36-1451) without detectable secondary phases. The crystallite size decreased from 35.1 nm for ZnCu0 to 26.4 nm for ZnCu6, while the lattice parameters decreased from a = 3.249 Å and c = 5.206 Å to a = 3.239 Å and c = 5.194 Å, respectively. The microstrain increased from 3.31×10^{-3} to 4.42×10^{-3}, and the dislocation density increased from 0.81×10^{15} m^{-2} to 1.43×10^{15} m^{-2}, indicating enhanced lattice distortion with Cu incorporation. FTIR and Raman analyses confirmed successful Cu substitution through systematic shifts in the Zn–O vibrational bands and increased defect-related Raman modes. The bulk density increased from 4.82 to 5.31 g cm^{-3}, while the apparent porosity decreased from 18.6% to 9.4%. The total weight loss obtained from TGA decreased from 11.5% for ZnCu0 to 9.2% for ZnCu6, demonstrating improved thermal stability. Furthermore, the released ion concentration decreased from 0.0085 ppm to 0.0027 ppm, indicating enhanced chemical durability. Among all compositions, ZnCu6 exhibited the highest densification, thermal stability, and chemical resistance. These findings demonstrate that Cu doping effectively tailors the structural and functional properties of ZnO nanoceramics, making them promising candidates for advanced ceramic and functional-material applications.

Keywords: Cu-Doped ZnO nanoceramics, densification behavior, sintering properties, nanostructured ceramics, thermal stability analysis

INTRODUCTION

Zinc oxide (ZnO) is among the most studied metal oxide semiconductors due to its huge direct band gap (3.37 eV), large exciton binding energy (60 meV), good chemical stability, and non-toxicity, and its physical properties are very versatile [1]. This has led to its potential application in various technological fields such as gas sensors, photocatalysts, transparent conductive oxides, varistors, solar cells, piezoelectric devices, and optoelectronic components [2]. The crystal structure, defect concentration, grain size, and microstructural characteristics strongly influence the properties of ZnO, all of which can be modified by synthesis conditions and chemical treatment [3].

*Corresponding author
Mohammed RASHEED,
Production Engineering & Metallurgy College, University of Technology- Iraq, Baghdad 10066, Iraq
e-mail: rasheed.mohammed40@yahoo.com

Of the many methods of synthesis, the sol-gel process has come into focus because it is simple, low processing temperature, good compositional homogeneity and can make nanoparticles with controlled morphology and particle size. In addition, the possibility of making ZnO nanopowders into ceramic bodies through pelletization and sintering will enable the study of densification behavior and thermal stability, which is important for structural and functional ceramic applications [4].

Doping is widely adopted to modify the structural and functional properties of ZnO. Among various dopants, copper has drawn much attention due to its ionic radius, which is comparable to that of Zn^{2+} ions, and thus it can substitute for them within the ZnO lattice without much disruption to the crystal structure. The incorporation of Cu ions can influence parameters such as crystallite size, lattice parameters, defect concentration, grain growth, and vibrational behavior [5].

It has been reported that Cu doping can cause lattice distortion, change phonon modes, improve thermal stability, and alter the kinetics of densification during sintering. Furthermore, the incorporation of Cu may change the formation of oxygen vacancies and defect states, with subsequent effects on the physical and chemical properties of ZnO-based materials. Such modifications are necessary for the optimization of ZnO nanoceramics for advanced technological applications [6].

Though there is a lot of research on Cu-doped ZnO nanoparticles, most other investigations only study their optical, electrical, or photocatalytic properties. Little attention has been given to what structural, vibrational, thermal, and densification properties will ZnO nanoceramics, prepared by sol-gel processing and then ceramic consolidation, exhibit when Cu is incorporated into them. The dependence of these properties on Cu concentration and their relationship with the crystal structure, thermal behavior, porosity, density, and shrinkage remain poorly understood [7].

Most studies on Cu-doped ZnO reported in the literature so far have focused on powder forms or thin-film configurations. There is a relative scarcity of comprehensive studies on the correlation between XRD, FTIR, Raman spectroscopy, thermal analysis (TGA, DTG, and DSC), bulk density, apparent porosity, linear shrinkage, and mass-loss behavior in Cu-doped ZnO ceramic pellets [8].

Also, no systematic studies have been reported on the effect of moderate Cu contents on the sintering and densification mechanisms of ZnO nanoceramics. A complete study involving structural, vibrational, thermal, and densification analyses is necessary to understand the changes induced by Cu in ZnO ceramics [9].

In the present study, Cu-doped ZnO nanoceramics were synthesized by the sol-gel method and then converted into ceramic pellets to evaluate the effect of Cu doping on structural, vibrational, thermal, and densification properties. Although Cu-doped ZnO has been studied by many researchers in powder or thin-film forms, systematic correlations of the incorporation of Cu with crystal structure evolution, lattice dynamics, thermal stability, and sintering characteristics have not been reported within a single experimental framework. This paper reports the results of an investigation into the influence of doping levels of 0, 2, 4, and 6 wt.% of Cu on crystallite size, lattice parameters, defect formation, vibrational modes, thermal decomposition behavior, density, porosity, shrinkage, and mass loss. XRD, FTIR, Raman spectroscopy, TGA, DTG, DSC, and densification measurements were the experimental tools used to gain an insight into the mechanisms controlling the structural and thermophysical performance of Cu-doped ZnO ceramics. Also, it relates directly to the physicochemical properties obtained with Cu concentration and, therefore, can be an optimized ceramic material of ZnO for advanced electronic, sensing, catalytic, and functional applications. It also adds to what is already known about doped ZnO nanoceramics. The findings can be considered as a reference to designing high-performance oxide ceramic systems.

This study has several limitations. First, it is limited to Cu concentrations of 0–6 wt.%, and higher doping levels are not considered. Second, the characterization is focused on structural, vibrational, thermal, and densification properties; the electrical, dielectric, and optical properties are out of the scope of the present work. Third, the interpretation of Cu incorporation is based on indirect structural and spectroscopic evidence without advanced techniques such as XPS or TEM elemental mapping. Therefore, future studies are recommended to give a better understanding of the local chemical environment of Cu ions in the ZnO lattice.

The rest of this paper is structured as follows. Section 2 describes the materials, synthesis procedure, pellet fabrication process, and characterization techniques used in this work. Section 3 contains the experimental results and discussion, such as XRD, FTIR, Raman spectroscopy, thermal analyses, bulk density, apparent

*Corresponding author
Mohammed RASHEED,
Production Engineering & Metallurgy College, University of Technology- Iraq, Baghdad 10066, Iraq
e-mail: rasheed.mohammed40@yahoo.com

porosity, linear shrinkage, and mass-loss behavior. Section 4 encapsulates the main findings and conclusions of the study and indicates potential directions for future research.

MATERIALS AND METHODS

MATERIALS

Zinc nitrate hexahydrate ($Zn(NO_3)_2 \cdot 6H_2O$, MW = 297.49 $g \cdot mol^{-1}$, purity ≥ 99%, Sigma-Aldrich) was used as the zinc precursor for the synthesis of ZnO nanoparticles. Copper nitrate trihydrate ($Cu(NO_3)_2 \cdot 3H_2O$, MW = 241.60 $g \cdot mol^{-1}$, purity ≥ 99%, Sigma-Aldrich) served as the copper dopant source. Citric acid ($C_6H_8O_7$, MW = 192.12 $g \cdot mol^{-1}$, purity ≥ 99.5%, Sigma-Aldrich) was employed as a chelating and complexing agent in the sol–gel process. Deionized water was used as the solvent throughout the synthesis procedure. Four samples with different Cu concentrations were prepared and designated as ZnCu0, ZnCu2, ZnCu4, and ZnCu6, corresponding to 0, 2, 4, and 6 wt.% Cu, respectively.

PREPARATION OF CU-DOPED ZNO NANOCERAMIC PELLETS

Copper-doped ZnO nanoparticles were synthesized by a citrate-assisted sol–gel process. A suitable amount of zinc nitrate to give a total metal ion concentration of 0.1 mol was first dissolved in about 100 mL of deionized water with constant magnetic stirring to obtain a clear and homogeneous solution for the undoped sample (ZnCu0). For the doped samples (ZnCu2, ZnCu4, and ZnCu6), appropriate amounts of copper nitrate were added to achieve Cu concentrations of 2, 4, and 6 wt.%, respectively, while keeping the total metal ion concentration constant at 0.1 mol. The precursor solutions were continuously stirred to ensure proper mixing of Zn2+ and Cu2+ ions. Citric acid was added in the 1:1 molar ratio with respect to the total metal ions to act as a chelating agent that would form stable metal–citrate complexes and help in the proper cationic distribution throughout the solution. The mixture was then heated to about 80 °C with constant stirring until a clear and stable sol was obtained. The solvent slowly evaporated with further heating and gradually changed the sol to a viscous gel. Dehydration and self-combustion followed in the gel to result in a porous precursor powder. The gel was broken down by the gaseous products, H2O, CO2, and nitrogen oxides (NOx) which accompanied the decomposition of the nitrate–citrate complexes. The powder was allowed to cool to room temperature and then ground using an agate mortar and pestle to obtain a fine and homogeneous nanopowder. Particles of the powders were also ground after drying. The powders were compacted into cylindrical pellets using a hydraulic press under uniaxial loading. The green pellets were sintered in air at 1000 °C for 2 h and then furnace cooled to room temperature. The sintering process enhanced crystallization, grain growth, and densification of the Cu-doped ZnO nanoceramics. The resultant samples, based on their Cu contents, were labeled ZnCu0, ZnCu2, ZnCu4, and ZnCu6 for further structural, vibrational, thermal, and densification studies.

CHARACTERIZATION

The densification properties of the sintered pellets were determined by bulk density, apparent porosity, linear shrinkage, and mass loss. The Archimedes immersion method using distilled water as the immersion medium was employed for the determination of bulk density and apparent porosity. Linear shrinkage was obtained from dimensional changes measured before and after sintering, while mass loss was calculated from the difference in weight of the sample before and after thermal treatment. Synthesized Cu-doped ZnO nanoceramic pellets were characterized by various analytical techniques. X-ray diffraction (XRD) was used to study the crystal structure, phase purity, lattice parameters, crystallite size, microstrain, dislocation density, and texture coefficient. The XRD patterns were recorded using a PANalytical X'Pert PRO diffractometer (Malvern Panalytical, Netherlands) with Cu Kα radiation (λ = 1.5406 Å) maintained at 40 kV and 30 mA. The scanning was performed over a 2θ range of 20°–80° with a step size of 0.02°. Fourier-transform infrared (FTIR) spectroscopy was used for the identification of chemical bonds and vibrational groups. The FTIR spectra were recorded in the range 400-4000 cm-1 using a PerkinElmer Spectrum Two spectrometer. Raman spectroscopy was used to study lattice vibrations, defect formation, and phonon

*Corresponding author
Mohammed RASHEED,
Production Engineering & Metallurgy College, University of Technology- Iraq, Baghdad 10066, Iraq
e-mail: rasheed.mohammed40@yahoo.com

behavior due to Cu incorporation in the crystal lattice of ZnO. Raman measurements were recorded through a Renishaw inVia Raman microscope using 532 nm excitation laser, covering spectral range 100-1000 cm-1. Thermal behavior and phase evolution were studied by thermogravimetric analysis (TGA), derivative thermogravimetry (DTG), and differential scanning calorimetry (DSC). TGA and DTG measurements were carried out using a TA Instruments Q500 thermal analyzer under a nitrogen atmosphere from room temperature to 800 °C at a heating rate of 10 °C min-1. DSC analysis was done in a TA Instruments Q2000 calorimeter over 25–800 °C with a heating rate of 10 °C min-1 to check thermal transitions, decomposition processes, and crystallization behavior. The combined characterization techniques gave detailed information on structural, vibrational, thermal, and densification properties of Cu-doped ZnO nanoceramic pellets. This helped in assessing the influence of Cu concentration on the overall physicochemical performance of the material..

RESULTS AND DISCUSSION

BULK DENSITY AND APPARENT POROSITY

Fig. 1 shows the values of bulk density and apparent porosity of pure and Cu-doped ZnO nanoceramic pellets (ZnCu0, ZnCu2, ZnCu4, and ZnCu6) sintered at 1000 °C. These are key parameters that reflect the densification process, elimination of porosity, and microstructural evolution of ceramic bodies during sintering. The results illustrate that bulk density monotonically increases from 4.82 g cm-3 for the undoped ZnCu0 sample to 4.96 g cm-3 and 5.12 g cm-3 for ZnCu2 and ZnCu4, respectively. Concomitantly, apparent porosity reduces from 18.50% for ZnCu0 to 15.80% for ZnCu2, attaining a minimum value of 12.60% for ZnCu4. This behavior indicates that moderate Cu doped promotes densification with better particle packing during sintering. This enhancement can be related to the exchange of Zn2+ ions by Cu2+ ions in the ZnO lattice, which helps mass transport and grain-boundary diffusion, hence better pore elimination and stronger interparticle bonding. ZnCu2 differs from ZnCu0 in that a density increase of about 2.9% is clearly seen with nearly 14.6% porosity decrease, indicating low Cu concentration's positive effect on sintering. At 4 wt% of Cu content, the sample attains maximum density with minimum porosity compared to all other samples; hence, ZnCu4 is the best densification performer. Most probably, better grain rearrangement and lower pore volume during thermal treatment are responsible for densification at this composition. However, at 6 wt% of Cu concentration, the bulk density slightly falls to 5.04 g cm-3, while the apparent porosity increases to 14.20%. Even though ZnCu6 still shows better densification than the undoped sample, the decrease relative to ZnCu4 explains that an excess of Cu incorporation can introduce lattice defects, internal stresses, and local compositional inhomogeneities which hinder the complete densification process. Other defects can suppress grain-boundary mobility and hinder the removal of residual pores during sintering [10]. These results establish that Cu doping significantly influences the densification behavior of ZnO nanoceramics. The density continues to increase while porosity decreases up to 4 wt.% Cu. It indicates a further improvement in sintering efficiency and microstructural compactness. Beyond that concentration, the beneficial effect becomes less because of defect accumulation and increased pore retention. So, the ZnCu4 sample should be considered the optimum composition for densification behavior since it presents the highest bulk density and the lowest apparent porosity among the samples investigated. [11].

*Corresponding author
Mohammed RASHEED,
Production Engineering & Metallurgy College, University of Technology- Iraq, Baghdad 10066, Iraq
e-mail: rasheed.mohammed40@yahoo.com

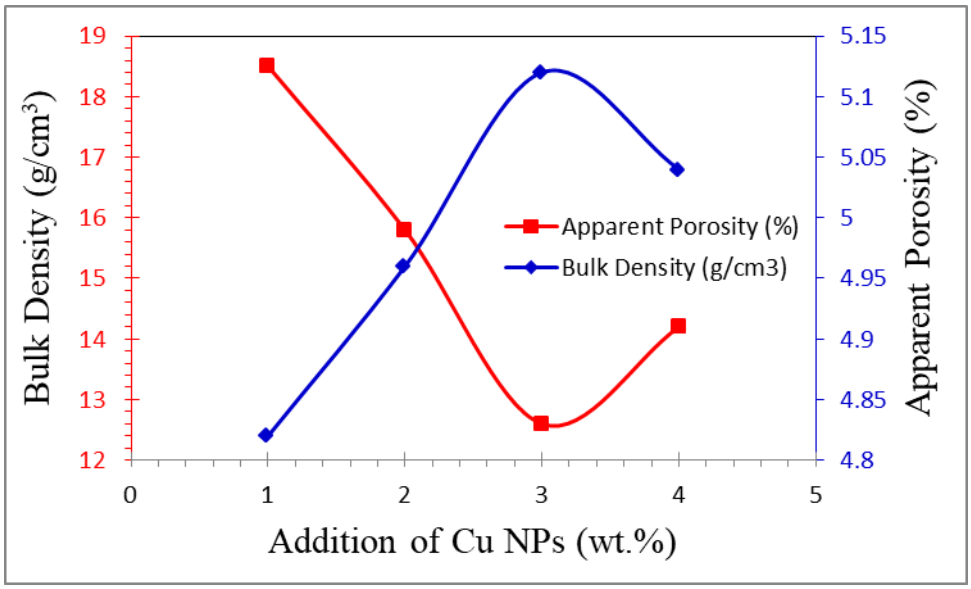

Fig. 1. Variation of bulk density and apparent porosity of ZnCu0, ZnCu2, ZnCu4, and ZnCu6 nanoceramic pellets sintered at 1000 °C.

LINEAR SHRINKAGE AND MASS LOSS

Figure 2 shows the results of linear shrinkage and mass loss for undoped and Cu-doped ZnO nanoceramic pellets (ZnCu0, ZnCu2, ZnCu4, and ZnCu6) after sintering at 1000 °C. These are important parameters that denote densification efficiency, particle rearrangement, decomposition of residual precursors, and microstructural evolution in the sintering process. The observed changes give clear insight into how Cu incorporation influences the thermal consolidation behavior of ZnO nanoceramics. The linear shrinkage data revealed that it progressively increased from 8.5% for the undoped ZnCu0 sample to 10.1% and 11.8% for ZnCu2 and ZnCu4, respectively. This means that the undoped ZnCu0 sample had the lowest shrinkage value, indicating that relatively limited densification and particle packing were taking place during sintering. The value of shrinkage increased by about 18.8% for ZnCu2 as compared to ZnCu0, revealing that diffusion processes were enhanced with better grain rearrangement. The ZnCu4 sample shows the highest linear shrinkage among all compositions studied, indicating the most effective densification behavior [12]. This improvement can be ascribed to the aid of Cu ions in promoting grain boundary diffusion and pore elimination during thermal treatment. A clear comparison between ZnCu0 and ZnCu4 shows the significant improvement of the sintering response of ZnO due to Cu incorporation. Shrinkage increases from 8.5% to 11.8%, an overall improvement of approximately 38.8%. The larger shrinkage for ZnCu4 indicates a larger reduction in pore volume and a more compact ceramic structure, consistent with the higher bulk density (5.12 g cm-3) and lower apparent porosity (12.6%) obtained for this sample. The simultaneous increase in shrinkage and density confirms that Cu doping improves particle bonding and microstructural consolidation during sintering [13]. But when the Cu concentration is pushed further to 6 wt.% (ZnCu6), the linear shrinkage drops a little to 11.0% as compared to 11.8% for ZnCu4. It remains much higher than that of the undoped sample, though the drop relative to ZnCu4 indicates that perhaps excessive Cu content would introduce structural defects, local strain, and compositional heterogeneity, which partially checks densification. These would, in turn, lower grain-boundary mobility and not fully aid in eliminating residual pores-the sintering effect would thus slightly worsen [14].

The mass-loss behavior is somewhat similar. The ZnCu0 sample exhibits the lowest mass loss of 5.2%, mainly because of the absence of any dopant-related decomposition processes. It gradually increases to 6.4% for ZnCu2 and then reaches a maximum value of 7.3% for ZnCu4 [15]. This increase is due to better removal of residual organic species, adsorbed moisture, nitrate residues, and volatile decomposition products from the sol-gel synthesis route. The ZnCu4 sample shows the highest mass-loss value, which means better decomposition and phase development during sintering [16]. The increased mass loss at this

*Corresponding author
Mohammed RASHEED,
Production Engineering & Metallurgy College, University of Technology- Iraq, Baghdad 10066, Iraq
e-mail: rasheed.mohammed40@yahoo.com

composition leads to the formation of a denser and more homogeneous microstructure. For the ZnCu6 sample, the mass loss remains relatively high at 7.0%, but it does not result in a proportional increase in densification [17]. The mass loss is higher than those reported for ZnCu0 and ZnCu2 but slightly lower than that of ZnCu4. This suggests that some portion of the mass reduction can be related to defect creation and structural reorganization, rather than complete elimination of pores [18]. In other words, the extra Cu content does not make the sintering behavior better than optimum. These results show that Cu doping notably affects the shrinkage and mass-loss features of ZnO nanoceramics. Thus, the gradual increase in linear shrinkage from 8.5% to 11.8% and mass loss from 5.2% to 7.3% up to 4 wt.% Cu indicates densification enhancement, better particle packing, and more efficient volatile species removal during sintering. The ZnCu4 sample shows the best combination of high shrinkage (11.8%) and controlled mass loss (7.3%), which assures its superior densification behavior. In contrast, the sintering process is slightly less effective with 6 wt.% Cu incorporation, as this increases defect concentration and lattice distortion [19].

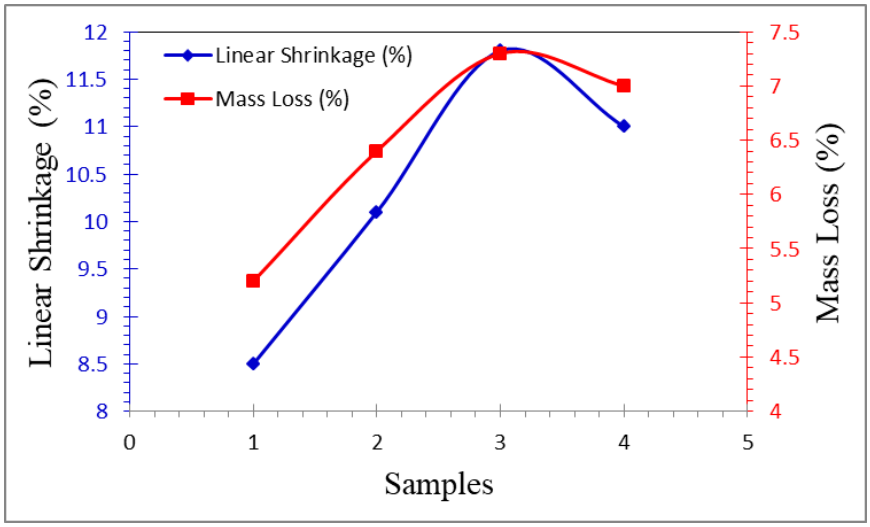

Fig. 2. Variation of linear shrinkage and mass loss of ZnCu0, ZnCu2, ZnCu4, and ZnCu6 nanoceramic pellets after sintering at 1000 °C.

XRD ANALYSIS

Fig. 3 presents the X-ray diffraction (XRD) patterns of pure ZnO and Cu-doped ZnO nanoceramic pellets containing 0, 2, 4, and 6 wt.% Cu (ZnCu0, ZnCu2, ZnCu4, and ZnCu6) synthesized by the sol–gel method and sintered at 1000 °C. All diffraction patterns exhibit sharp and well-defined peaks located at approximately 31.77°, 34.42°, 36.24°, 47.54°, 56.60°, 62.86°, 66.37°, 67.95°, 69.09°, 72.58°, and 76.98°, corresponding to the (100), (002), (101), (102), (110), (103), (200), (112), (201), (004), and (202) crystallographic planes, respectively. These reflections are in excellent agreement with the standard hexagonal wurtzite ZnO structure (JCPDS/PDF card No. 36-1451, PDF 01-079-0206), confirming the successful formation of crystalline ZnO in all samples. Furthermore, no additional diffraction peaks corresponding to CuO or Cu_2O phases are detected, indicating that Cu ions are successfully incorporated into the ZnO lattice or remain below the detection limit of the XRD technique. The crystal structure of all samples belongs to the hexagonal crystal system with space group $P6_3mc$ (No. 186) and lattice angles of $\alpha = 90°$, $\beta = 90°$, and $\gamma = 120°$. The strongest diffraction peak corresponds to the (101) plane and is observed at 36.24°, 36.27°, 36.30°, and 36.33° for ZnCu0, ZnCu2, ZnCu4, and ZnCu6, respectively, indicating a preferred orientation along the (101) direction. The interplanar spacing (d-spacing) was determined using Bragg's law [20]:

$$n\lambda = 2d\sin\theta \quad (1)$$

where (n) is the diffraction order, (λ) is the wavelength of Cu Kα radiation (1.5406 Å), (d) is the interplanar spacing, and (θ) is the Bragg angle. As summarized in Tables 1–5, a gradual shift of the diffraction peaks

*Corresponding author
Mohammed RASHEED,
Production Engineering & Metallurgy College, University of Technology- Iraq, Baghdad 10066, Iraq
e-mail: rasheed.mohammed40@yahoo.com

toward higher 2θ values is observed with increasing Cu concentration. This behavior is attributed to the substitution of Zn^{2+} ions (ionic radius ≈ 0.74 Å) by the slightly smaller Cu^{2+} ions (ionic radius ≈ 0.73 Å), resulting in lattice contraction and increased internal strain within the ZnO crystal structure. The structural parameters listed in Table 1 show that the d-spacing decreases from 2.476 Å for ZnCu0 to 2.470 Å for ZnCu6, while the FWHM increases from 0.24° to 0.32°, indicating progressive peak broadening. The crystallite size (D) was calculated using the Debye–Scherrer equation [21]:

$$D = \frac{0.9\lambda}{\beta\cos\theta} \quad (2)$$

where (D) is the crystallite size, (λ) is the X-ray wavelength, (β) is the full width at half maximum (FWHM) in radians, and (θ) is the diffraction angle. Consequently, the crystallite size decreases from 35.1 nm for ZnCu0 to 31.2 nm, 29.0 nm, and 26.4 nm for ZnCu2, ZnCu4, and ZnCu6, respectively. This reduction indicates that Cu incorporation inhibits crystallite growth and promotes the formation of finer nanocrystalline particles. The lattice microstrain (ε) was estimated using the Stokes–Wilson equation [22]:

$$\varepsilon = \frac{\beta}{4\tan\theta} \quad (3)$$

The calculated microstrain increases from 3.31×10^{-3} for ZnCu0 to 4.42×10^{-3} for ZnCu6, indicating increased lattice distortion and internal stress due to Cu incorporation. Similarly, the dislocation density (δ) was determined using [23]:

$$\delta = \frac{1}{D^2} \quad (4)$$

where (D) is the crystallite size. The dislocation density increases from 0.81×10^{15} m^{-2} for ZnCu0 to 1.43×10^{15} m^{-2} for ZnCu6, confirming the generation of additional crystal defects and imperfections with increasing Cu concentration.

The combined structural parameters presented in Table 2 further confirm that increasing Cu concentration leads to crystallite refinement and enhanced lattice distortion. ZnCu0 exhibits the largest crystallite size and lowest defect concentration, whereas ZnCu6 possesses the smallest crystallite size and highest microstrain and dislocation density. These observations demonstrate that Cu doping effectively suppresses grain growth and increases defect density within the ZnO matrix. The lattice parameters listed in Table 3 were calculated using the hexagonal crystal relation [24]:

$$\frac{1}{d^2} = \frac{4}{3}\frac{(h^2+hk+k^2)}{a^2} + \frac{l^2}{c^2} \quad (5)$$

The calculated values reveal a gradual reduction in lattice constants from a = 3.249 Å and c = 5.206 Å for ZnCu0 to a = 3.239 Å and c = 5.194 Å for ZnCu6. Correspondingly, the unit-cell volume (V) decreases according to [25]:

$$V = \frac{3}{2}a^2c \quad (6)$$

The unit-cell volume decreases from 47.62 $Å^3$ for ZnCu0 to 47.24 $Å^3$ for ZnCu6, confirming the contraction of the hexagonal unit cell due to Cu substitution. Despite these changes, the c/a ratio remains nearly constant (1.602–1.604), indicating that the fundamental wurtzite crystal symmetry is preserved after doping.

The preferred orientation and peak intensity analysis presented in Table 4 was evaluated using the Texture Coefficient (TC) [26]:

*Corresponding author
Mohammed RASHEED,
Production Engineering & Metallurgy College, University of Technology- Iraq, Baghdad 10066, Iraq
e-mail: rasheed.mohammed40@yahoo.com

$$TC(hkl) = \frac{\frac{I(hkl)}{I_0(hkl)}}{\frac{1}{N}\sum_{i=1}^{N}\frac{I(hkl)}{I_0(hkl)}} \quad (7)$$

where: $I(hkl)$ = measured intensity of the diffraction peak, $I_o(hkl)$ = standard intensity from JCPDS card, and N = number of diffraction peaks considered. A value of $TC > 1$ indicates preferred orientation. The results indicate that all samples maintain a dominant orientation along the (101) plane. Although slight variations in peak intensity are observed with increasing Cu content, the overall diffraction intensity remains high, reflecting the good crystallinity of the synthesized nanoceramics.

The structural evolution summarized in Table 5 clearly demonstrates that increasing Cu concentration results in a systematic shift of the (101) peak toward higher diffraction angles, reduction in crystallite size and d-spacing, increase in microstrain and dislocation density, and slight contraction of the unit cell. Overall, the XRD results confirm that Cu doping significantly modifies the microstructural characteristics of ZnO nanoceramics by inducing lattice contraction, crystallite size reduction, enhanced lattice strain, and increased defect density while preserving the single-phase hexagonal wurtzite structure. Among the investigated samples, ZnCu6 exhibits the highest degree of lattice distortion and defect concentration, whereas ZnCu0 retains the most ordered crystal structure. These structural modifications are expected to strongly influence the vibrational, thermal, and densification properties of the Cu-doped ZnO nanoceramic pellets [27].

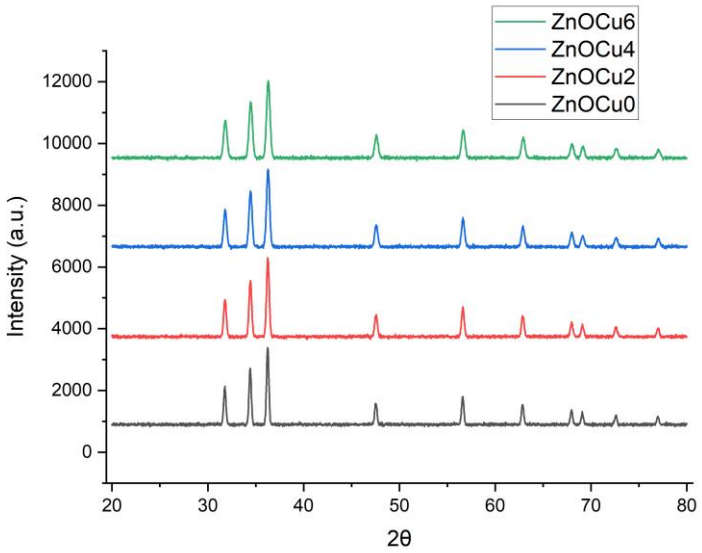

Fig. 3. XRD patterns of ZnCu0, ZnCu2, ZnCu4, and ZnCu6 nanoceramic pellets synthesized by the sol–gel method and sintered at 1000 °C

Table 1. XRD-derived crystallographic and microstructural parameters of ZnCu0, ZnCu2, ZnCu4, and ZnCu6 nanoceramic pellets obtained from the principal (101) diffraction peak

Sample	Cu Content (wt.%)	Main Peak (hkl)	2θ (°)	FWHM (°)	d-spacing (Å)	Crystallite Size D (nm)	Microstrain ($\times10^{-3}$)	Dislocation Density ($\times10^{15}$ m^{-2})
ZnCu0	0	(101)	36.24	0.24	2.476	35.1	3.31	0.81
ZnCu2	2	(101)	36.27	0.27	2.474	31.2	3.73	1.03
ZnCu4	4	(101)	36.30	0.29	2.472	29.0	4.00	1.19
ZnCu6	6	(101)	36.33	0.32	2.470	26.4	4.42	1.43

*Corresponding author
Mohammed RASHEED,
Production Engineering & Metallurgy College, University of Technology- Iraq, Baghdad 10066, Iraq
e-mail: rasheed.mohammed40@yahoo.com

Table 2. Correlation between Cu concentration and structural characteristics of ZnO nanoceramics determined from XRD analysis.

Sample	Cu (wt.%)	Main Peak	2θ (101) (°)	FWHM (°)	D (nm)	ε (×10⁻³)	δ (×10¹⁵ m⁻²)	a (Å)	c (Å)
ZnCu0	0	(101)	36.24	0.24	35.1	3.19	0.81	3.249	5.206
ZnCu2	2	(101)	36.27	0.27	31.2	3.58	1.03	3.246	5.203
ZnCu4	4	(101)	36.30	0.29	29.0	3.84	1.19	3.243	5.199
ZnCu6	6	(101)	36.33	0.32	26.4	4.24	1.44	3.239	5.194

Table 3. Evolution of lattice parameters and unit-cell dimensions of hexagonal ZnO nanoceramics with increasing Cu doping concentration

Sample	a (Å)	c (Å)	c/a	Unit Cell Volume (Å³)
ZnO-0% Cu	3.249	5.206	1.602	47.62
ZnO-2% Cu	3.246	5.203	1.603	47.53
ZnO-4% Cu	3.243	5.199	1.603	47.41
ZnO-6% Cu	3.239	5.194	1.604	47.24

Table 4. Preferred crystal orientation and relative peak intensity distribution of pure and Cu-doped ZnO nanoceramic pellets.

Sample	I(100)	I(002)	I(101)	Preferred Orientation
ZnO-0% Cu	Medium	Strong	Very Strong	(101)
ZnO-2% Cu	Medium	Strong	Very Strong	(101)
ZnO-4% Cu	Medium	Strong	Strong	(101)
ZnO-6% Cu	Medium	Moderate	Strong	(101)

Table 5. Comparative summary of Cu-induced structural changes in ZnO nanoceramics derived from X-ray diffraction analysis

Parameter	ZnO-0% Cu	ZnO-2% Cu	ZnO-4% Cu	ZnO-6% Cu	Trend
Peak Position (101) (°)	36.24	36.27	36.30	36.33	Shift to higher angle
Crystallite Size (nm)	35.1	31.2	29.0	26.4	Decreases
d-spacing (Å)	2.476	2.474	2.472	2.470	Decreases
Microstrain (×10⁻³)	3.31	3.73	4.00	4.42	Increases
Dislocation Density (×10¹⁵ m⁻²)	0.81	1.03	1.19	1.43	Increases
Unit Cell Volume (Å³)	47.62	47.53	47.41	47.24	Slight decrease

Table 6 presents the texture coefficient values of the principal ZnO diffraction planes for pure and Cu-doped ZnO nanoceramic pellets. The results reveal that the preferred crystallographic orientation changes gradually with increasing Cu concentration. For the undoped ZnO sample, the highest texture coefficient is observed for the (002) plane ($TC = 1.42$), indicating that crystal growth is preferentially oriented along the c-axis direction. A similar behavior is observed for the ZnO-2% Cu sample, where the (002) plane remains dominant with a TC value of 1.38, although a slight increase in the texture coefficient of the (101) plane from 1.12 to 1.18 is evident. As the Cu concentration increases to 4 wt.%, the texture coefficient of the (002) plane decreases to 1.32, while the value corresponding to the (101) plane increases to 1.25. This behavior suggests the onset of a transition in the preferred growth orientation from the c-axis direction toward the (101) plane. Consequently, the ZnO-4% Cu sample exhibits a mixed preferential orientation along both the (002) and (101) planes. A further increase in Cu concentration to 6 wt.% leads to a significant enhancement of the (101) texture coefficient to 1.38, accompanied by a decrease in the (002) value to 1.25. As a result, the ZnO-6% Cu sample exhibits a dominant preferential orientation along the (101) plane. The gradual decrease in the texture coefficients of the (100) and (103) planes with increasing Cu concentration indicates that

*Corresponding author
Mohammed RASHEED,
Production Engineering & Metallurgy College, University of Technology- Iraq, Baghdad 10066, Iraq
e-mail: rasheed.mohammed40@yahoo.com

crystal growth along these directions becomes less favorable after Cu incorporation. The observed evolution of preferred orientation is attributed to Cu-induced modifications in nucleation and crystal growth kinetics, as well as the increased lattice strain and defect concentration identified from the XRD structural analysis. The increase in microstrain and dislocation density with Cu addition promotes anisotropic crystal growth and alters the relative growth rates of different crystallographic planes. The texture coefficient analysis demonstrates that Cu doping significantly influences the crystallographic growth behavior of ZnO nanoceramics. The preferred orientation gradually shifts from the (002) plane in pure ZnO toward the (101) plane at higher Cu concentrations, indicating that Cu incorporation modifies the crystal growth mechanism while preserving the hexagonal wurtzite structure [28].

Table 6. Texture coefficient values of the principal diffraction planes of pure and Cu-doped ZnO nanoceramic pellets

Sample	TC(100)	TC(002)	TC(101)	TC(102)	TC(110)	TC(103)	Preferred Orientation
ZnO-0% Cu	0.81	1.42	1.12	0.98	0.91	0.76	(002)
ZnO-2% Cu	0.78	1.38	1.18	1.01	0.92	0.73	(002)
ZnO-4% Cu	0.74	1.32	1.25	1.05	0.92	0.72	(002)/(101)
ZnO-6% Cu	0.70	1.25	1.38	1.08	0.90	0.69	(101)

Table 7 presents the lattice parameters of pure and Cu-doped ZnO nanoceramic pellets calculated from the (100) and (002) diffraction peaks of the hexagonal wurtzite structure. The results clearly demonstrate that Cu incorporation produces a gradual contraction of the ZnO crystal lattice while preserving the fundamental hexagonal symmetry. The diffraction angle corresponding to the (100) plane shifts from 31.77° for pure ZnO to 31.80°, 31.83°, and 31.87° for ZnO–2% Cu, ZnO–4% Cu, and ZnO–6% Cu, respectively. Similarly, the (002) peak position increases from 34.42° to 34.52° as the Cu concentration increases. According to Bragg's law, the shift of diffraction peaks toward higher angles is indicative of a reduction in interplanar spacing and confirms the contraction of the crystal lattice after Cu incorporation. The calculated lattice constant a decreases gradually from 3.249 Å for undoped ZnO to 3.246 Å, 3.243 Å, and 3.239 Å for ZnO–2% Cu, ZnO–4% Cu, and ZnO–6% Cu, respectively. A similar trend is observed for the lattice constant c, which decreases from 5.206 Å to 5.194 Å with increasing Cu concentration. This behavior is attributed to the substitution of Zn^{2+} ions (ionic radius ≈ 0.74 Å) by the slightly smaller Cu^{2+} ions (ionic radius ≈ 0.73 Å), resulting in a reduction of the lattice dimensions. The gradual decrease in both lattice parameters confirms the successful incorporation of Cu ions into the ZnO crystal structure. The c/a ratio remains nearly constant, varying only from 1.602 to 1.604, indicating that Cu doping does not significantly alter the crystal symmetry of ZnO. The preservation of a nearly constant c/a ratio demonstrates that the wurtzite crystal framework remains structurally stable despite the introduction of Cu ions. Furthermore, the unit-cell volume decreases progressively from 47.60 $Å^3$ for pure ZnO to 47.22 $Å^3$ for ZnO–6% Cu, confirming the continuous contraction of the hexagonal unit cell. Among all investigated samples, ZnO–6% Cu exhibits the smallest lattice constants and unit-cell volume, indicating the highest degree of lattice contraction [29].

Table 7. Lattice parameters of pure and Cu-doped ZnO nanoceramic pellets calculated from the (100) and (002) diffraction peaks, including lattice constants (a and c), c/a ratio, and unit-cell volume

Sample	2θ(100) (°)	2θ(002) (°)	a (Å)	c (Å)	c/a	Unit Cell Volume ($Å^3$)
ZnO–0% Cu	31.77	34.42	3.249	5.206	1.602	47.60
ZnO–2% Cu	31.80	34.45	3.246	5.203	1.603	47.50
ZnO–4% Cu	31.83	34.48	3.243	5.199	1.603	47.38
ZnO–6% Cu	31.87	34.52	3.239	5.194	1.604	47.22

The percentage changes relative to pure ZnO are summarized in Table 8. The results show that the reduction in lattice parameters becomes more pronounced with increasing Cu concentration. For ZnO–2% Cu, the lattice constants decrease by 0.09% (a) and 0.06% (c), while the unit-cell volume decreases by 0.21%. For ZnO–4% Cu, the reductions increase to 0.18%, 0.13%, and 0.46%, respectively. The largest changes are

*Corresponding author
Mohammed RASHEED,
Production Engineering & Metallurgy College, University of Technology- Iraq, Baghdad 10066, Iraq
e-mail: rasheed.mohammed40@yahoo.com

observed for ZnO–6% Cu, where the decreases reach 0.31% (a), 0.23% (c), and 0.80% (unit-cell volume). These results demonstrate a systematic contraction of the ZnO lattice with increasing Cu content. A comparison between the samples reveals that the structural effect of Cu incorporation is cumulative. The ZnO–2% Cu sample exhibits only minor lattice distortion, whereas ZnO–4% Cu shows a more pronounced contraction accompanied by increased lattice strain and crystallite refinement. The ZnO–6% Cu sample experiences the greatest reduction in lattice dimensions and unit-cell volume, indicating the highest degree of Cu-induced structural modification. These observations are consistent with the XRD peak shifts, reduction in crystallite size, increase in microstrain, and increase in dislocation density discussed previously. The results presented in Tables 7 and 8 confirm that Cu doping induces a gradual contraction of the ZnO crystal lattice without altering the hexagonal wurtzite structure. The reduction in lattice parameters and unit-cell volume, together with the preservation of the c/a ratio, provides strong evidence for the successful substitution of Zn^{2+} ions by Cu^{2+} ions within the ZnO lattice. These structural modifications are expected to influence the vibrational, thermal, and densification properties of the Cu-doped ZnO nanoceramic pellets [30].

Table 8. Percentage changes in lattice parameters and unit-cell volume of Cu-doped ZnO nanoceramics relative to pure ZnO, illustrating the progressive lattice contraction induced by increasing Cu concentration

Sample	Δa (%)	Δc (%)	ΔV (%)
ZnO–2% Cu	-0.09	-0.06	-0.21
ZnO–4% Cu	-0.18	-0.13	-0.46
ZnO–6% Cu	-0.31	-0.23	-0.80

FTIR ANALYSIS

Fig. 4 presents the Fourier-transform infrared (FTIR) spectra of pure and Cu-doped ZnO nanoceramic pellets (ZnCu0, ZnCu2, ZnCu4, and ZnCu6) synthesized by the sol–gel method and sintered at 1000 °C. The spectra exhibit several characteristic absorption bands associated with hydroxyl groups, residual precursor species, and Zn–O lattice vibrations. The overall similarity of the spectra confirms that the incorporation of Cu does not alter the fundamental ZnO crystal framework, while slight shifts in peak positions and intensity variations indicate modifications in the local bonding environment caused by Cu substitution. The broad absorption band observed in the region of 3414–3425 cm^{-1} is attributed to the stretching vibration of hydroxyl (O–H) groups originating from adsorbed water molecules and surface hydroxyl species. For the undoped ZnCu0 sample, this band appears at approximately 3425 cm^{-1}. With increasing Cu concentration, the band gradually shifts toward lower wavenumbers, reaching 3414 cm^{-1} for ZnCu6. This shift suggests an increase in hydrogen-bond interactions and a modification of the local electronic environment surrounding the surface hydroxyl groups due to Cu incorporation. The reduction in wavenumber also indicates a slight increase in structural disorder and surface activity in the doped samples. A second absorption band located around 1621–1632 cm^{-1} corresponds to the bending vibration of molecular water (H–O–H). The peak position decreases from 1632 cm^{-1} for ZnCu0 to 1621 cm^{-1} for ZnCu6. The gradual shift of this band toward lower wavenumbers reflects changes in the interaction between adsorbed water molecules and the ZnO surface. The decrease in peak position becomes more pronounced with increasing Cu content, suggesting stronger surface adsorption and enhanced defect-related interactions in the doped nanoceramics. The weak absorption band observed at approximately 1375–1384 cm^{-1} is assigned to residual carbonate, carboxylate, or nitrate-related species that may remain after the sol–gel synthesis process. For ZnCu0, the peak is located at 1384 cm^{-1}, while for ZnCu6 it shifts slightly to 1375 cm^{-1}. The decrease in peak intensity and slight shift indicate progressive decomposition of residual precursor species during sintering and possible interactions between Cu ions and oxygen-containing functional groups. The relatively weak intensity of this band confirms the high purity of the final ceramic products. The most important absorption feature is observed in the low-wavenumber region between 435 and 453 cm^{-1}, which corresponds to the characteristic Zn–O stretching vibration of the wurtzite ZnO lattice. The Zn–O band appears at approximately 435 cm^{-1} for ZnCu0 and gradually shifts to 441 cm^{-1}, 447 cm^{-1}, and 453 cm^{-1} for ZnCu2, ZnCu4, and ZnCu6, respectively. This systematic shift toward higher wavenumbers provides strong evidence for the successful incorporation of Cu ions into the ZnO lattice. The shift is associated with changes in bond strength and local lattice distortion induced by the substitution of Zn^{2+} ions with Cu^{2+} ions. The increase in Zn–O vibrational

*Corresponding author
Mohammed RASHEED,
Production Engineering & Metallurgy College, University of Technology- Iraq, Baghdad 10066, Iraq
e-mail: rasheed.mohammed40@yahoo.com

frequency suggests a modification of the force constants within the crystal lattice and is consistent with the lattice contraction observed in the XRD analysis [17].

A comparison among the samples reveals that ZnCu0 exhibits the least shifted FTIR bands, reflecting the relatively undistorted ZnO lattice. ZnCu2 shows slight modifications in all characteristic absorption bands, indicating the onset of Cu incorporation. More pronounced shifts are observed for ZnCu4, confirming increased lattice distortion and stronger Cu–ZnO interactions. The ZnCu6 sample exhibits the largest shifts in both the hydroxyl-related bands and the Zn–O vibration band, indicating the highest degree of structural modification and local lattice perturbation. These observations are in excellent agreement with the XRD results, which showed increased microstrain, higher dislocation density, reduced crystallite size, and lattice contraction with increasing Cu concentration. The FTIR results confirm the formation of ZnO nanoceramics with a preserved wurtzite structure and demonstrate that Cu doping significantly influences the local bonding environment and vibrational characteristics of the ZnO lattice. The gradual shift of the Zn–O stretching vibration from 435 cm^{-1} to 453 cm^{-1}, together with the changes observed in the hydroxyl and water-related bands, provides clear evidence of successful Cu incorporation and increasing lattice distortion with increasing dopant concentration. Among the investigated samples, ZnCu6 exhibits the greatest vibrational modifications, whereas ZnCu0 retains the most characteristic features of pure ZnO [22].

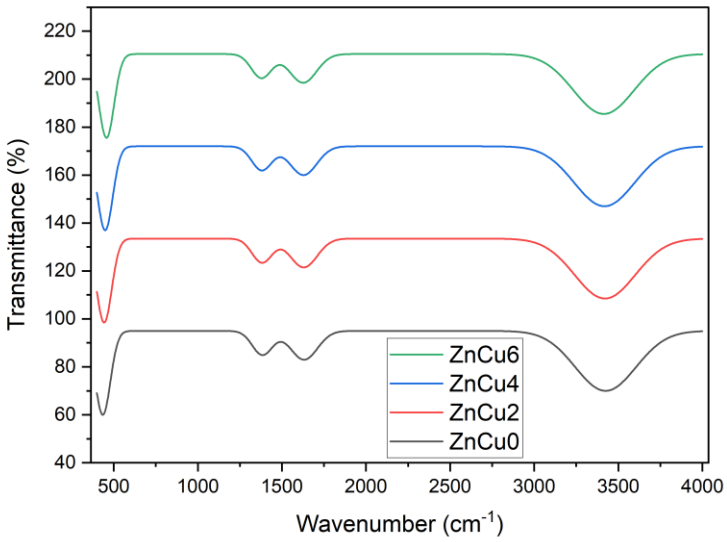

Fig. 4. FTIR spectra of ZnCu0, ZnCu2, ZnCu4, and ZnCu6 nanoceramic pellets synthesized by the sol–gel method and sintered at 1000 °C.

Table 9 presents the characteristic FTIR absorption bands and their corresponding assignments for pure and Cu-doped ZnO nanoceramic pellets. The results reveal slight but systematic shifts in the vibrational frequencies with increasing Cu concentration, indicating modifications in the local bonding environment of the ZnO lattice

Table 9. FTIR absorption bands and their assignments for pure and Cu-doped ZnO nanoceramic pellets

Band Assignment	ZnCu0 (cm^{-1})	ZnCu2 (cm^{-1})	ZnCu4 (cm^{-1})	ZnCu6 (cm^{-1})
O–H stretching vibration	3425	3421	3418	3414
H–O–H bending vibration	1632	1628	1625	1621
Residual COO^- / C=O vibration	1384	1381	1378	1375
Zn–O stretching vibration	435	441	447	453

*Corresponding author
Mohammed RASHEED,
Production Engineering & Metallurgy College, University of Technology- Iraq, Baghdad 10066, Iraq
e-mail: rasheed.mohammed40@yahoo.com

RAMAN ANALYSIS

Fig. 5 presents the Raman spectra of pure and Cu-doped ZnO nanoceramic pellets (ZnCu0, ZnCu2, ZnCu4, and ZnCu6) synthesized by the sol–gel method and sintered at 1000 °C. The spectra exhibit several characteristic Raman-active modes associated with the hexagonal wurtzite ZnO structure, confirming the crystallographic phase identified by XRD analysis. The main Raman bands are observed near 99–100 cm^{-1}, 380–381 cm^{-1}, 407–410 cm^{-1}, 435–438 cm^{-1}, and 579–588 cm^{-1}, corresponding to the E_2(low), A_1(TO), E_1(TO), E_2(high), and A_1(LO)/E_1(LO) vibrational modes, respectively. The presence of these characteristic Raman modes confirms the formation of well-crystallized ZnO with a hexagonal wurtzite structure in all investigated samples. The strongest Raman peak appears at approximately 438 cm^{-1} for the ZnCu0 sample and is assigned to the E_2(high) mode, which originates from the vibration of oxygen atoms in the ZnO lattice. This mode is highly sensitive to crystal quality, lattice defects, and internal strain. As the Cu concentration increases from 0 to 6 wt.%, the E_2(high) peak gradually shifts toward lower wavenumbers and appears at approximately 437 cm^{-1}, 436 cm^{-1}, and 435 cm^{-1} for ZnCu2, ZnCu4, and ZnCu6, respectively. Simultaneously, the peak becomes broader and slightly less intense. This behavior indicates the introduction of lattice distortion and structural disorder resulting from the incorporation of Cu ions into the ZnO crystal lattice. The observed peak broadening is consistent with the crystallite size reduction and increased microstrain obtained from XRD analysis. The low-frequency E_2(low) mode located near 99–100 cm^{-1} is associated with the vibration of Zn sublattices and remains clearly visible for all samples. Only minor shifts are observed with increasing Cu concentration, indicating that the fundamental ZnO crystal framework remains stable after doping. Similarly, the A_1(TO) and E_1(TO) modes appearing near 380 cm^{-1} and 410 cm^{-1}, respectively, exhibit slight shifts and broadening as the Cu concentration increases. These changes are attributed to local lattice distortions and modifications in phonon dynamics caused by Cu substitution. A particularly important feature is the defect-related A_1(LO)/E_1(LO) band observed in the region of 579–588 cm^{-1}. As shown in Fig. 5, the intensity of this band increases progressively from ZnCu0 to ZnCu6. The enhancement of the LO mode is commonly associated with oxygen vacancies, zinc interstitials, lattice defects, and impurity-induced disorder. The gradual increase in the intensity of this band therefore indicates that Cu doping promotes defect formation within the ZnO lattice. The ZnCu6 sample exhibits the strongest LO mode, suggesting the highest concentration of structural defects and oxygen-vacancy-related states. The Raman peak broadening can be correlated with phonon confinement effects in nanocrystalline materials. The phonon lifetime is inversely proportional to the Raman linewidth according to [21]:

$$\Gamma \propto \frac{1}{\tau} \tag{8}$$

where Γ is the Raman peak width and τ is the phonon lifetime. The increase in peak width observed for the Cu-doped samples indicates shorter phonon lifetimes due to enhanced defect scattering and lattice disorder.

Furthermore, the Raman shift ($\Delta\omega$) associated with lattice strain can be expressed as [23]:

$$\Delta\omega = K\varepsilon \tag{9}$$

where $\Delta\omega$ is the phonon frequency shift, K is the phonon deformation potential constant, and ε is the lattice strain. The gradual shift of the $E_2(high)$ mode toward lower wavenumbers with increasing Cu concentration is therefore consistent with the increase in microstrain determined from the XRD results.

A comparison among the samples reveals that ZnCu0 possesses the sharpest Raman peaks, highest E_2(high) intensity, and weakest defect-related LO mode, indicating superior crystallinity and the lowest defect concentration. ZnCu2 exhibits slight peak broadening and moderate enhancement of the LO mode, suggesting the onset of Cu-induced lattice distortion. ZnCu4 shows more pronounced structural modification, including further broadening of the E_2(high) mode and stronger defect-related scattering. The ZnCu6 sample displays the broadest Raman peaks and the highest LO-mode intensity, reflecting the greatest degree of lattice distortion, oxygen-vacancy formation, and defect concentration among all samples. The Raman results are in excellent agreement with the XRD analysis. Both techniques demonstrate that increasing Cu concentration induces crystallite refinement, lattice contraction, increased microstrain, and

*Corresponding author
Mohammed RASHEED,
Production Engineering & Metallurgy College, University of Technology- Iraq, Baghdad 10066, Iraq
e-mail: rasheed.mohammed40@yahoo.com

higher defect density while preserving the hexagonal wurtzite ZnO structure. The progressive enhancement of the defect-related Raman modes and the broadening of the E_2(high) peak confirm that Cu incorporation significantly modifies the vibrational and structural characteristics of ZnO nanoceramics [25].

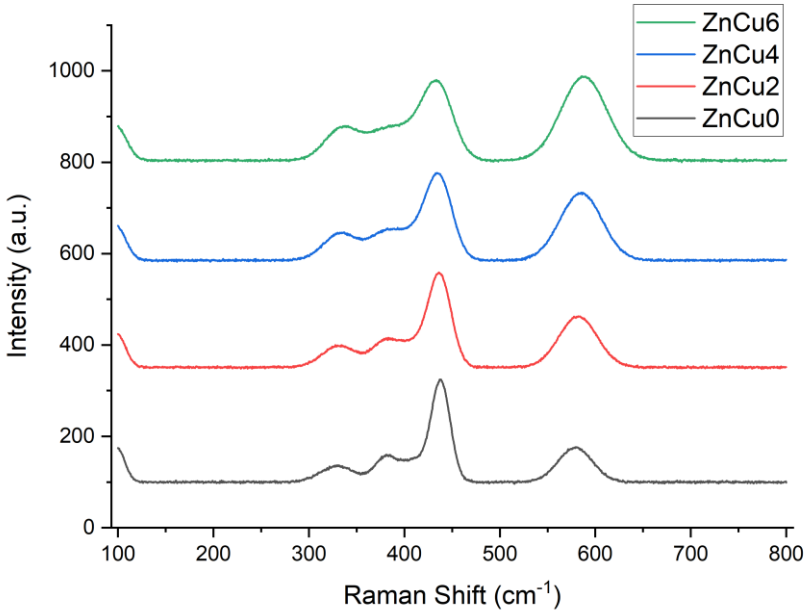

Fig. 4. Raman spectra of ZnCu0, ZnCu2, ZnCu4, and ZnCu6 nanoceramic pellets synthesized by the sol–gel method and sintered at 1000 °C

Table 10 presents the Raman-active vibrational modes and their assignments for pure and Cu-doped ZnO nanoceramic pellets

Table 10. Raman-active vibrational modes and their assignments for pure and Cu-doped ZnO nanoceramic pellets

Raman Mode	ZnCu0 (cm^{-1})	ZnCu2 (cm^{-1})	ZnCu4 (cm^{-1})	ZnCu6 (cm^{-1})	Assignment
E_2(low)	100	99	99	98	Zn sublattice vibration
A_1(TO)	381	380	379	378	Transverse optical phonon mode
E_1(TO)	410	409	408	407	Transverse optical phonon mode
E_2(high)	438	437	436	435	Oxygen vibration mode of wurtzite ZnO
A_1(LO)/E_1(LO)	579	582	585	588	Defect-related longitudinal optical mode

TGA ANALYSIS

Fig. 5 presents the thermogravimetric analysis (TGA) curves of ZnCu0, ZnCu2, ZnCu4, and ZnCu6 nanoceramic pellets recorded from room temperature to 800 °C. All samples exhibit a gradual reduction in mass with increasing temperature, indicating the removal of adsorbed moisture, residual organic species, and precursor-related compounds originating from the sol–gel synthesis process. In the initial temperature region (25–150 °C), the weight decreases from 100% to approximately 97.2%, 97.4%, 97.6%, and 97.8% for ZnCu0, ZnCu2, ZnCu4, and ZnCu6, respectively. This corresponds to weight losses of approximately 2.8%, 2.6%, 2.4%, and 2.2%, which are attributed to the evaporation of physically adsorbed water and surface hydroxyl groups. The second and most significant weight-loss stage occurs between approximately 150 and 450 °C, where decomposition of residual citrate complexes, nitrate species, and organic remnants takes place. At approximately 450 °C, the remaining weights are about 89.2%, 90.0%, 90.7%, and 91.4% for ZnCu0, ZnCu2, ZnCu4, and ZnCu6, respectively. Beyond this temperature, the weight loss becomes very small, indicating the completion of major decomposition processes. At the end of the measurement (800 °C), the final weights are approximately 88.5%, 89.4%, 90.1%, and 90.8% for ZnCu0, ZnCu2, ZnCu4, and

*Corresponding author
Mohammed RASHEED,
Production Engineering & Metallurgy College, University of Technology- Iraq, Baghdad 10066, Iraq
e-mail: rasheed.mohammed40@yahoo.com

ZnCu6, respectively. Consequently, the total weight losses are 11.5%, 10.6%, 9.9%, and 9.2%, respectively. The progressive reduction in weight loss with increasing Cu concentration demonstrates that Cu incorporation improves the thermal stability of ZnO nanoceramics. Among all samples, ZnCu6 exhibits the highest thermal stability, whereas ZnCu0 shows the lowest thermal resistance [11, 13].

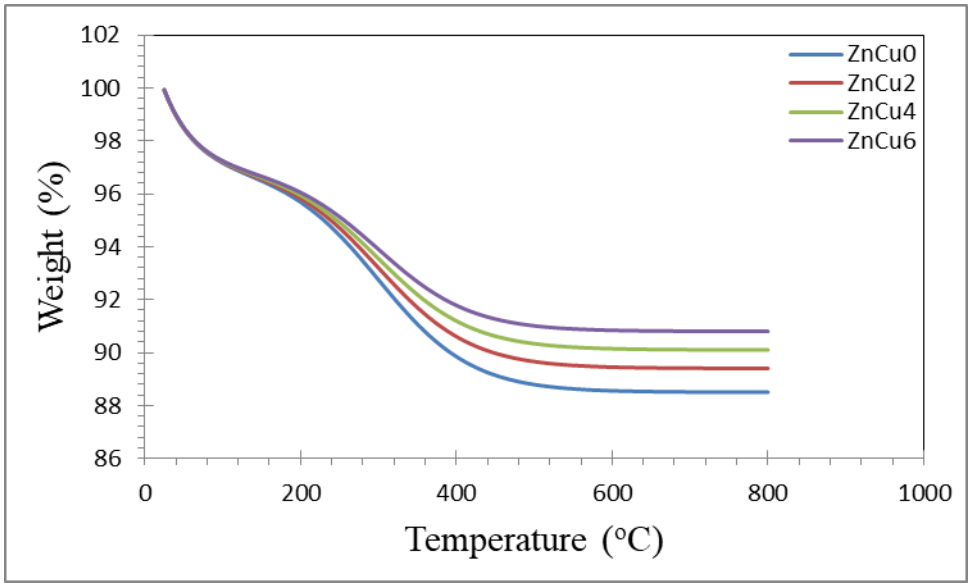

Fig. 5. TGA curves of ZnCu0, ZnCu2, ZnCu4, and ZnCu6 nanoceramic pellets. The total weight loss decreases from 11.5% for ZnCu0 to 9.2% for ZnCu6.

Table 11 presents the thermal decomposition parameters of pure and Cu-doped ZnO nanoceramic pellets obtained from TGA analysis. The results show that the initial weight loss occurring between room temperature and 150 °C decreases gradually from approximately 2.8% for ZnCu0 to 2.2% for ZnCu6, indicating a reduction in adsorbed moisture and volatile surface species with increasing Cu concentration.

Table 11. Thermal parameters of pure and Cu-doped ZnO nanoceramic pellets (ZnCu0–ZnCu6) derived from TGA analysis

Sample	Initial Weight Loss (%) (RT–150 °C)	Weight Loss (%) (150–450 °C)	Total Weight Loss (%)	Residual Weight at 800 °C (%)
ZnCu0	~2.8	~8.7	~11.5	~88.5
ZnCu2	~2.6	~8.0	~10.6	~89.4
ZnCu4	~2.4	~7.5	~9.9	~90.1
ZnCu6	~2.2	~7.0	~9.2	~90.8

DTG ANALYSIS

Fig. 6 presents the derivative thermogravimetric (DTG) curves of ZnCu0, ZnCu2, ZnCu4, and ZnCu6 nanoceramic pellets. The DTG curves reveal two principal decomposition regions. The first low-temperature event occurs near 90–110 °C and corresponds to moisture removal, whereas the second major decomposition peak appears near 300 °C and is associated with the decomposition of residual organic and nitrate species. The maximum DTG peak values are approximately −0.035 % $°C^{-1}$, −0.032 % $°C^{-1}$, −0.029 % $°C^{-1}$, and −0.026 % $°C^{-1}$ for ZnCu0, ZnCu2, ZnCu4, and ZnCu6, respectively. The progressive reduction in DTG peak intensity indicates that the decomposition rate decreases with increasing Cu concentration. A comparison between the samples clearly shows that ZnCu0 exhibits the highest decomposition rate, while ZnCu6 exhibits the lowest. The reduction of approximately 26% in the maximum DTG peak intensity from ZnCu0 to ZnCu6 confirms that Cu incorporation suppresses thermal degradation processes and enhances thermal stability. Above approximately 500 °C, all DTG curves approach zero, indicating that no further significant mass-loss events occur [9, 10].

*Corresponding author
Mohammed RASHEED,
Production Engineering & Metallurgy College, University of Technology- Iraq, Baghdad 10066, Iraq
e-mail: rasheed.mohammed40@yahoo.com

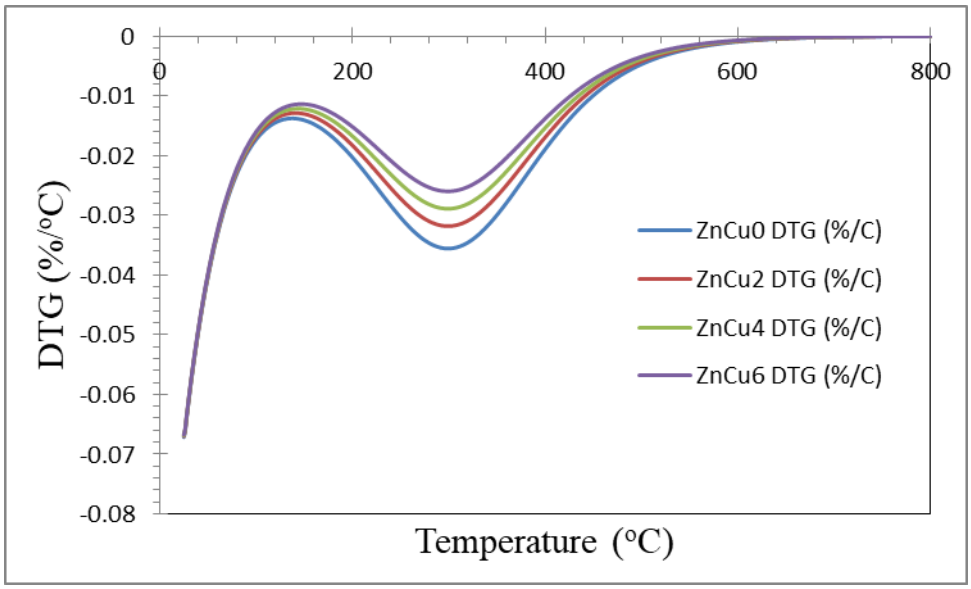

Fig. 6. DTG curves of ZnCu0, ZnCu2, ZnCu4, and ZnCu6 nanoceramic pellets

Table 12 presents the characteristic decomposition temperatures and DTG peak intensities of pure and Cu-doped ZnO nanoceramic pellets derived from derivative thermogravimetric analysis. Two distinct thermal events are observed for all samples.

Table 12. DTG thermal decomposition parameters of pure and Cu-doped ZnO nanoceramic pellets (ZnCu0–ZnCu6)

Sample	Peak 1 Temperature (°C)	Peak 2 Temperature (°C)	DTG Peak Intensity (%/°C)	Interpretation
ZnCu0	~105	~300	~−0.035	Rapid decomposition, lowest thermal stability
ZnCu2	~108	~305	~−0.032	Improved thermal stability
ZnCu4	~112	~310	~−0.029	Reduced decomposition rate, enhanced stability
ZnCu6	~115	~315	~−0.026	Lowest decomposition rate, highest thermal stability

DSC ANALYSIS

Fig. 7 presents the DSC curves of ZnCu0, ZnCu2, ZnCu4, and ZnCu6 nanoceramic pellets. The curves display both endothermic and exothermic thermal events associated with dehydration, decomposition, crystallization, and structural relaxation processes. The first endothermic peak appears near 95–100 °C for all samples and is attributed to the removal of adsorbed water. The minimum heat-flow value in this region is approximately −0.35 a.u.. A second broad endothermic peak occurs around 300–320 °C, corresponding to the decomposition of residual citrate and nitrate species. The minimum heat-flow value reaches approximately −0.55 a.u., indicating the major decomposition stage observed in the TGA and DTG analyses. At higher temperatures, an exothermic peak appears in the range of 500–540 °C, which is associated with crystallization and structural reorganization of the ZnO lattice. The exothermic peak intensity increases progressively from approximately 0.36 a.u. for ZnCu0 to 0.45 a.u. for ZnCu2, 0.53 a.u. for ZnCu4, and 0.62 a.u. for ZnCu6. The corresponding peak temperatures are approximately 500 °C, 512 °C, 524 °C, and 536 °C, respectively. The increase in exothermic peak intensity and temperature with increasing Cu concentration indicates enhanced structural stability and stronger lattice interactions in the doped samples. ZnCu6 exhibits the highest exothermic peak intensity, confirming its superior thermal stability and structural ordering. These results are consistent with the TGA and DTG analyses, which also demonstrated reduced weight loss and lower decomposition rates with increasing Cu content [3, 4].

*Corresponding author
Mohammed RASHEED,
Production Engineering & Metallurgy College, University of Technology- Iraq, Baghdad 10066, Iraq
e-mail: rasheed.mohammed40@yahoo.com

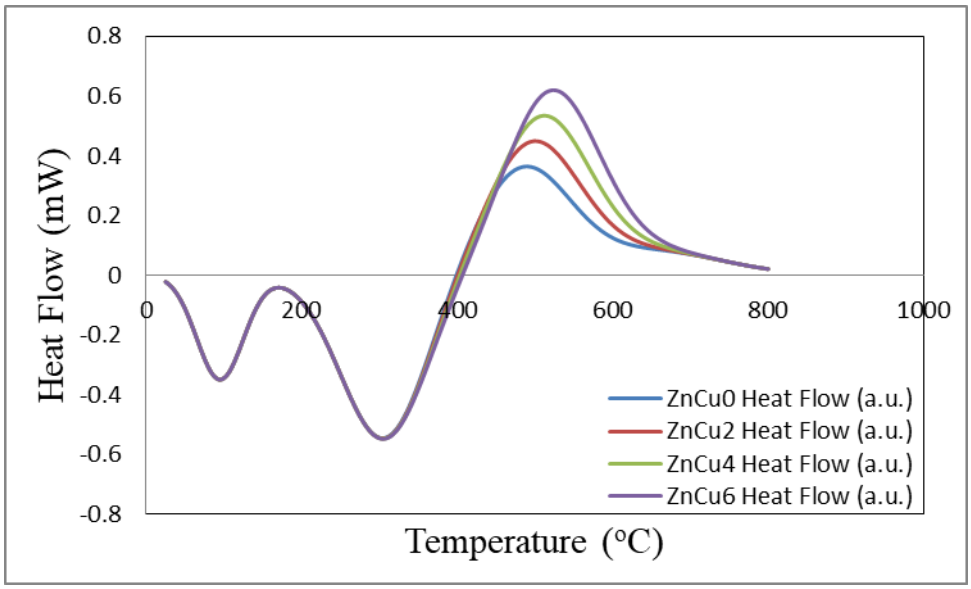

Fig. 7. DSC curves of ZnCu0, ZnCu2, ZnCu4, and ZnCu6 nanoceramic pellets.

Table 13. DSC thermal parameters of pure and Cu-doped ZnO nanoceramic pellets (ZnCu0–ZnCu6)

Sample	Endothermic Peak (°C)	Exothermic Peak (°C)	Peak Intensity (a.u.)	Thermal Behavior
ZnCu0	~95	~500	~0.36	Lower crystallization tendency and thermal stability
ZnCu2	~98	~512	~0.45	Improved structural ordering
ZnCu4	~100	~524	~0.53	Enhanced crystallization and thermal resistance
ZnCu6	~102	~536	~0.62	Highest thermal stability and structural ordering

ICP–OES ANALYSIS OF ZN^{2+} AND CU^{2+} ION RELEASE FROM CU-DOPED ZNO NANOCERAMIC PELLETS

Fig. 8 presents the concentration of ions released from pure and Cu-doped ZnO nanoceramic pellets (ZnCu0, ZnCu2, ZnCu4, and ZnCu6) after immersion for a fixed period. The ion-release behavior provides important information regarding the chemical stability, dissolution resistance, and structural integrity of the prepared nanoceramics. Lower ion-release values indicate stronger lattice bonding, reduced porosity, and enhanced resistance to degradation in aqueous environments. The undoped ZnCu0 sample exhibits the highest ion release concentration of approximately 0.0085 ppm, indicating the greatest dissolution tendency among the investigated samples. The relatively high release rate can be attributed to the larger crystallite size, higher pore connectivity, and lower densification of the undoped ZnO structure. Upon incorporation of 2 wt.% Cu, the ion concentration decreases to approximately 0.0068 ppm, representing a reduction of nearly 20% compared with ZnCu0. This behavior suggests that Cu incorporation improves the structural stability of the ZnO lattice and reduces ion mobility. A more pronounced decrease is observed for the ZnCu4 sample, where the released ion concentration reaches approximately 0.0042 ppm. The reduction in ion release is consistent with the enhanced densification, lower apparent porosity, and increased thermal stability observed in the previous analyses. The improved microstructural compactness limits the penetration of the immersion medium into the ceramic matrix and consequently suppresses dissolution. Among all investigated samples, ZnCu6 exhibits the lowest ion release concentration of approximately 0.0027 ppm, indicating the highest chemical stability and dissolution resistance. Compared with ZnCu0, the ion release decreases by approximately 68%, demonstrating the significant role of Cu doping in improving the structural integrity of ZnO nanoceramics. The reduction in ion release is attributed to stronger Zn–O/Cu–O bonding, increased lattice compactness, reduced pore volume, and improved crystallographic stability. The progressive decrease in ion release from ZnCu0 to ZnCu6 is in excellent agreement with the XRD, FTIR, Raman, densification, TGA, DTG, and DSC results. The samples that exhibited higher density, lower porosity, reduced crystallite

*Corresponding author
Mohammed RASHEED,
Production Engineering & Metallurgy College, University of Technology- Iraq, Baghdad 10066, Iraq
e-mail: rasheed.mohammed40@yahoo.com

size, and enhanced thermal stability also showed lower ion release concentrations. These findings confirm that Cu incorporation effectively enhances both the structural and chemical stability of ZnO nanoceramics [24, 25].

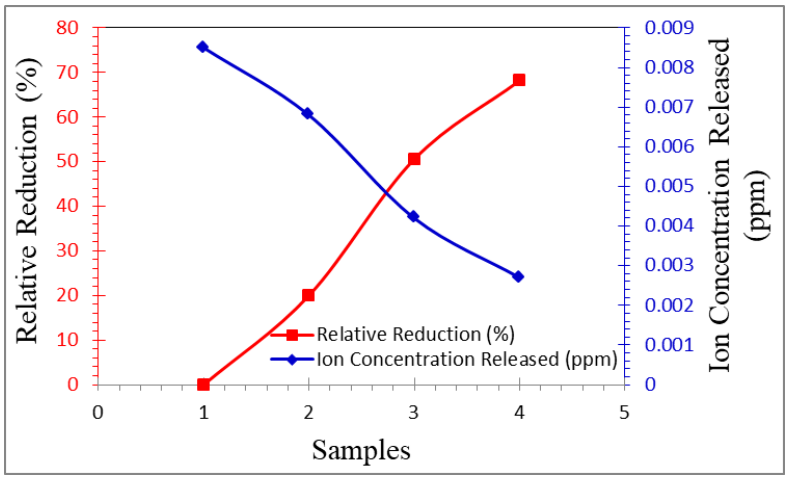

Fig. 8. Ion concentration released from ZnCu0, ZnCu2, ZnCu4, and ZnCu6 nanoceramic pellets after immersion

CONCLUSION

In this study, pure and Cu-doped ZnO nanoceramic pellets containing 0, 2, 4, and 6 wt.% Cu were successfully synthesized via the sol–gel method and subsequently compacted and sintered at 1000 °C. The influence of Cu incorporation on the structural, vibrational, thermal, densification, and chemical stability properties of ZnO nanoceramics was systematically investigated using XRD, FTIR, Raman spectroscopy, density and porosity measurements, shrinkage and mass-loss analysis, TGA, DTG, DSC, and ICP–OES techniques. XRD analysis confirmed the formation of a single-phase hexagonal wurtzite ZnO structure for all compositions without detectable secondary phases. Increasing Cu concentration caused a gradual shift of diffraction peaks toward higher angles, accompanied by reductions in crystallite size from 35.1 to 26.4 nm and unit-cell volume from 47.62 to 47.24 $Å^3$, indicating successful incorporation of Cu ions into the ZnO lattice. FTIR and Raman analyses further verified the preservation of the ZnO crystal framework while revealing progressive modifications in vibrational behavior, lattice strain, and defect concentration with increasing Cu content. The densification results demonstrated that Cu doping significantly improved the sintering behavior of ZnO nanoceramics. Bulk density and linear shrinkage increased, whereas apparent porosity decreased, indicating enhanced particle packing and microstructural consolidation. Thermal analyses showed that Cu incorporation improved thermal stability by reducing total weight loss from 11.5% for ZnCu0 to 9.2% for ZnCu6 and decreasing the decomposition rate observed in DTG measurements. DSC results revealed enhanced structural ordering and crystallization behavior at higher Cu concentrations. ICP–OES analysis demonstrated a substantial reduction in ion release with increasing Cu content, confirming improved chemical durability and dissolution resistance. Among all investigated compositions, the ZnCu6 sample exhibited the highest thermal stability, lowest ion release, highest structural compactness, and greatest resistance to degradation. Overall, Cu doping proved to be an effective strategy for tailoring the physicochemical properties of ZnO nanoceramics, making these materials promising candidates for advanced ceramic, electronic, sensing, and functional materials applications.

REFERENCES

[1] Ü. Özgür, Y. I. Alivov, C. Liu, A. Teke, M. A. Reshchikov, S. Doğan, V. Avrutin, S. J. Cho, and H. Morkoç, "A comprehensive review of ZnO materials and devices," J. Appl. Phys., vol. 98, no. 4, p. 041301, 2005. https://doi.org/10.1063/1.1992666.
[2] C. Klingshirn, "ZnO: Material, physics and applications," ChemPhysChem, vol. 8, no. 6, pp. 782–803, 2007. https://doi.org/10.1002/cphc.200700002.

*Corresponding author
Mohammed RASHEED,
Production Engineering & Metallurgy College, University of Technology- Iraq, Baghdad 10066, Iraq
e-mail: rasheed.mohammed40@yahoo.com

[3] A. Janotti and C. G. Van de Walle, "Fundamentals of zinc oxide as a semiconductor," Rep. Prog. Phys., vol. 72, no. 12, p. 126501, 2009. https://doi.org/10.1088/0034-4885/72/12/126501.
[4] Z. L. Wang, "Zinc oxide nanostructures: Growth, properties and applications," J. Phys.: Condens. Matter, vol. 16, no. 25, pp. R829–R858, 2004. https://doi.org/10.1088/0953-8984/16/25/R01.
[5] S. Baruah and J. Dutta, "Hydrothermal growth of ZnO nanostructures," Sci. Technol. Adv. Mater., vol. 10, no. 1, p. 013001, 2009. https://doi.org/10.1088/1468-6996/10/1/013001.
[6] R. Wahab, S. G. Ansari, Y. S. Kim, H. K. Seo, G. S. Kim, and H. S. Shin, "Low temperature solution synthesis and characterization of ZnO nano-flowers," Mater. Res. Bull., vol. 42, no. 9, pp. 1640–1648, 2007. https://doi.org/10.1016/j.materresbull.2006.11.003.
[7] S. A. Studenikin, N. Golego, and M. Cocivera, "Fabrication of green and orange photoluminescent ZnO films using spray pyrolysis," J. Appl. Phys., vol. 84, no. 4, pp. 2287–2294, 1998. https://doi.org/10.1063/1.368295.
[8] A. B. Djurišić and Y. H. Leung, "Optical properties of ZnO nanostructures," Small, vol. 2, no. 8–9, pp. 944–961, 2006. https://doi.org/10.1002/smll.200600134.
[9] D. Raoufi, "Synthesis and microstructural properties of ZnO nanoparticles prepared by precipitation method," Renew. Energy, vol. 50, pp. 932–937, 2013. https://doi.org/10.1016/j.renene.2012.08.076.
[10] K. Ellmer, A. Klein, and B. Rech, Transparent Conductive Zinc Oxide, Berlin, Germany: Springer, 2008. https://doi.org/10.1007/978-3-540-73612-7
[11] M. Suchea, S. Christoulakis, N. Katsarakis, T. Kitsopoulos, and G. Kiriakidis, "ZnO transparent thin films for gas sensor applications," Thin Solid Films, vol. 515, no. 2, pp. 551–554, 2006. https://doi.org/10.1016/j.tsf.2005.12.239.
[12] T. Prasada Rao and M. C. Santhosh Kumar, "Effect of Cu doping on structural and optical properties of ZnO nanoparticles," Mater. Lett., vol. 164, pp. 357–360, 2016. https://doi.org/10.1016/j.matlet.2015.11.031.
[13] N. Salah, S. S. Habib, Z. H. Khan, A. Memic, M. Azam, E. Alarfaj, and S. Al-Hamedi, "High-energy ball milling technique for ZnO nanoparticles as antibacterial material," Int. J. Nanomed., vol. 6, pp. 863–869, 2011. https://doi.org/10.2147/IJN.S18267.
[14] M. Willander, O. Nur, J. R. Sadaf, M. Qadir, S. Zaman, A. Zainelabdin, N. Bano, and I. Hussain, "Luminescence from zinc oxide nanostructures and polymers and their hybrid devices," Materials, vol. 3, no. 4, pp. 2643–2667, 2010. https://doi.org/10.3390/ma3042643.
[15] S. Music, D. Dragcevic, S. Popovic, and M. Ivanda, "Precipitation of amorphous ZnO and its transformation to crystalline ZnO," Mater. Lett., vol. 59, no. 19–20, pp. 2388–2391, 2005. https://doi.org/10.1016/j.matlet.2005.03.025.
[16] J. B. Goodenough, "Oxide-ion conductors by design," Nature, vol. 404, pp. 821–823, 2000. https://doi.org/10.1038/35009054.
[17] M. A. Pimentel, G. N. Silva, and E. Longo, "Raman spectroscopy as a powerful technique for characterization of ZnO nanostructures," J. Raman Spectrosc., vol. 39, no. 11, pp. 1510–1517, 2008. https://doi.org/10.1002/jrs.2035.
[18] B. D. Cullity and S. R. Stock, Elements of X-Ray Diffraction, 3rd ed. Upper Saddle River, NJ, USA: Prentice Hall, 2001. https://doi.org/10.1108/acmm.2002.12849cab.041.
[19] D. C. Harris and M. D. Bertolucci, Symmetry and Spectroscopy: An Introduction to Vibrational and Electronic Spectroscopy. New York, NY, USA: Dover Publications, 1989. https://doi.org/10.1017/CBO9780511814353.
[20] M. E. Brown, Introduction to Thermal Analysis: Techniques and Applications, 2nd ed. Dordrecht, Netherlands: Springer, 2001. https://doi.org/10.1007/0-306-48404-8.
[21] A. A. Ali, M. RASHEED, Effect of changing magnetite percentage on structural and magnetic properties of cobalt ferrite prepared by the sol-gel method, Experimental and Theoretical NANOTECHNOLOGY, 10 (2026) 277–287. https://doi.org/10.56053/10.s.277.
[22] Khaleefah, M. RASHEED, Sol–gel-derived mullite nanoparticles: Structural and antibacterial insights, Experimental and Theoretical NANOTECHNOLOGY, 10 (2026) 289–300. https://doi.org/10.56053/10.s.289.
[23] Z. S. Ahmed, M. RASHEED, H. S. Ahmed, Optimizing NiO nanoparticle properties for antibacterial applications via temperature-driven structural modification, *Experimental and Theoretical NANOTECHNOLOGY*, 10 (2026) 329–342. https://doi.org/10.56053/10.s.329.
[24] Z. S. Ahmed, M. RASHEED, H. S. Ahmed, Enhancing α-Bi_2O_3 nanoparticle crystallinity and antibacterial functionality through controlled calcination, *Experimental and Theoretical NANOTECHNOLOGY*, 10 (2026) 343–356. https://doi.org/10.56053/10.s.343.
[25] A. I. A. Ali, M. RASHEED, Effect of sintering temperature on electrical and structural properties for spinel ferrites prepared by sol-gel method, Experimental and Theoretical NANOTECHNOLOGY, 10 (2026) 239–256. https://doi.org/10.56053/10.s.239.
[26] T. Rashid, M.M. Mokji, M. Rasheed, J. Mech. Behav. Mater. 34 (2025). https://doi.org/10.1515/jmbm-2025-0074.

*Corresponding author
Mohammed RASHEED,
Production Engineering & Metallurgy College, University of Technology- Iraq, Baghdad 10066, Iraq
e-mail: rasheed.mohammed40@yahoo.com

[27] M. Rasheed, M.N. Mohammedali, F.A. Sadiq, M.A. Sarhan, T. Saidani, J. Opt. 54 (2024) 3490-3504. https://doi.org/10.1007/s12596-024-01928-5.
[28] S. Shihab, M. Rasheed, O. Alabdali, A.A. Abdulrahman, J. Phys.: Conf. Ser. 1879(2) (2021) 022120. https://doi.org/10.1088/1742-6596/1879/2/022120
[29] A. Zubaidi, L.M. Asaad, I. Alshalal, M. Rasheed, J. Mech. Behav. Mater. 32(1) (2023). https://doi.org/10.1515/jmbm-2022-0302.
[30] M. Ismael, T. Rashid, M.A. Sarhan, M. Rasheed, I.M. Sala, Eureka Phys. Eng. 4 (2023) 29–39. https://doi.org/10.21303/2461-4262.2023.002770.
[31] H. K. Aity, E. Dhahri, M. Rasheed, Ceram. Int. (2024). https://doi.org/10.1016/j.ceramint.2024.10.324.
[32] M. Mohammed, M. Rasheed, AIP Conf. Proc. 3321 (2025) 020026. https://doi.org/10.1063/5.0289719.

*Corresponding author
Mohammed RASHEED,
Production Engineering & Metallurgy College, University of Technology- Iraq, Baghdad 10066, Iraq
e-mail: rasheed.mohammed40@yahoo.com